PHYSICAL SCIENCE

Butterfly magnetoresistance, quasi-2D Dirac Fermi surface and topological phase transition in ZrSiS

Mazhar N. Ali,[1,2]* Leslie M. Schoop,[3] Chirag Garg,[1,2] Judith M. Lippmann,[3] Erik Lara,[1] Bettina Lotsch,[3,4] Stuart S. P. Parkin[1,2]

Magnetoresistance (MR), the change of a material's electrical resistance in response to an applied magnetic field, is a technologically important property that has been the topic of intense study for more than a quarter century. We report the observation of an unusual "butterfly"-shaped titanic angular magnetoresistance (AMR) in the nonmagnetic Dirac material, ZrSiS, which we find to be the most conducting sulfide known, with a 2-K resistivity as low as 48(4) nΩ·cm. The MR in ZrSiS is large and positive, reaching nearly 1.8 × 10^5 percent at 9 T and 2 K at a 45° angle between the applied current (*I* || *a*) and the applied field (90° is *H* || *c*). Approaching 90°, a "dip" is seen in the AMR, which, by analyzing Shubnikov de Haas oscillations at different angles, we find to coincide with a very sharp topological phase transition unlike any seen in other known Dirac/Weyl materials. We find that ZrSiS has a combination of two-dimensional (2D) and 3D Dirac pockets comprising its Fermi surface and that the combination of high-mobility carriers and multiple pockets in ZrSiS allows for large property changes to occur as a function of angle between applied fields. This makes it a promising platform to study the physics stemming from the coexistence of 2D and 3D Dirac electrons as well as opens the door to creating devices focused on switching between different parts of the Fermi surface and different topological states.

INTRODUCTION

Unconventional magnetoresistive behavior typically falls into the realm of magnetic materials, displaying negative magnetoresistance (MR) effects like giant MR and colossal MR. The MR is defined as

$$\mathrm{MR} = \frac{\rho(H) - \rho(0)}{\rho(0)}$$

where $\rho(H)$ is the resistivity in an applied field H, and is usually a very small effect in nonmagnetic materials, following the $(1 + \mu H^2)$ law, where μ is the carrier mobility. However, the MR behavior of Dirac and Weyl materials has recently been under investigation since the discovery of titanic MR in the type II Weyl semimetal (WSM) WTe_2 (*1*) as well as of linear MR and negative MR in the Dirac semimetals (DSMs) Na_3Bi and Cd_3As_2 and the type I WSM NbP, among others (*2*–*5*). Dirac line node materials, such as ZrSiTe and $PtSn_4$, are also of recent interest (*6*, *7*). Dirac and Weyl materials are an extremely popular area of research in condensed matter physics and solid-state chemistry because of their exotic fundamental physics and relatively easy syntheses. These materials have shown exciting properties, including extremely large carrier mobilities (*3*), titanic MR (*1*), and chiral anomaly (*2*).

The focus on MR measurements has partially been due to the ability to measure Shubnikov de Haas (SdH) oscillations and thereby gain insight into the size and shape of the Fermi surface of these semimetals. In metals and semimetals, the energy of the highest occupied level, which is termed the Fermi energy, lies within the energy range of one or more partially filled bands. For each partially filled band in reciprocal space (E versus k), there is a surface that separates the occupied and unoccupied levels. The sum of these surfaces is the Fermi surface. Insulators and semiconductors have no Fermi surface (ideally), whereas metals have differently shaped Fermi surfaces, which are intimately related to their transport properties (*8*).

SdH oscillations are oscillations in the electrical resistance of a material with increasing applied magnetic field strength. These oscillations are caused by the quantization of closed electronic orbits in a magnetic field, which are the extremal orbits around tubes or pockets in the Fermi surface. The frequency of the oscillations can be related to the size of the electronic orbit through the Onsager relationship, and quantities such as the Berry phase, an indicator of the topological state, can be extracted using the Lifshitz-Kosevich theory (*9*). The dependence of the SdH oscillations on the applied field angle can be used to understand the anisotropy of the Fermi surface, and in some cases, the complete angular magnetoresistance (AMR) profile combined with angle-dependent SdH measurements can be used to map out the Fermi surface (*8*, *10*). Studies of the AMR profiles of several Dirac/Weyl materials have found them to be typical of three-dimensional (3D) Fermi surfaces. Even WTe_2, which is a layered van der Waals material and structurally highly anisotropic, has a very 3D electronic structure, as evidenced by its moderate resistive anisotropy (*11*).

ZrSiS, a tetragonal PbFCl-type compound, was recently discovered by Schoop *et al.* (*12*) [and investigated by others (*13*–*15*)] to be a Dirac material, with several Dirac electron and hole pockets comprising its Fermi surface. ZrSiS is unique among the current set of Dirac/Weyl materials for several reasons: It is the first example of a "backyard" Dirac/Weyl material, which is composed of cheap, nontoxic, earth-abundant elements. It is also stable in air and water and is easy to grow crystals of. Electronically, it has a quasi-2D electronic structure. Density functional theory (DFT) calculations show that ZrSiS's Fermi surface is entirely made up of pockets created by linearly dispersed Dirac bands, resulting in a mixture of diamond-shaped pockets and more tubular ones (aligned with k_z and visible in Fig. 1). There is a nondegenerate Dirac nodal line formed by Dirac points along Γ-*M* and Γ-*X* as well as a nodal line formed by Dirac points along *Z*-*A* and *Z*-*R*. Also, angle-resolved photoemission spectroscopy revealed an unusual quasi-2D surface state with bulk hybridization (*12*).

[1]IBM Almaden Research Center, 650 Harry Road, San Jose, CA 95120, USA. [2]Max Planck Institute of Microstructure Physics, Weinberg 2, 06120 Halle, Germany. [3]Max Planck Institute for Solid State Research, Heisenbergstasse 1, 70569 Stuttgart, Germany. [4]Department of Chemistry, Ludwig-Maximilians-Universität München, Butenandtstrasse 5-13, 81377 München, Germany.
*Corresponding author. Email: maz@berkeley.edu

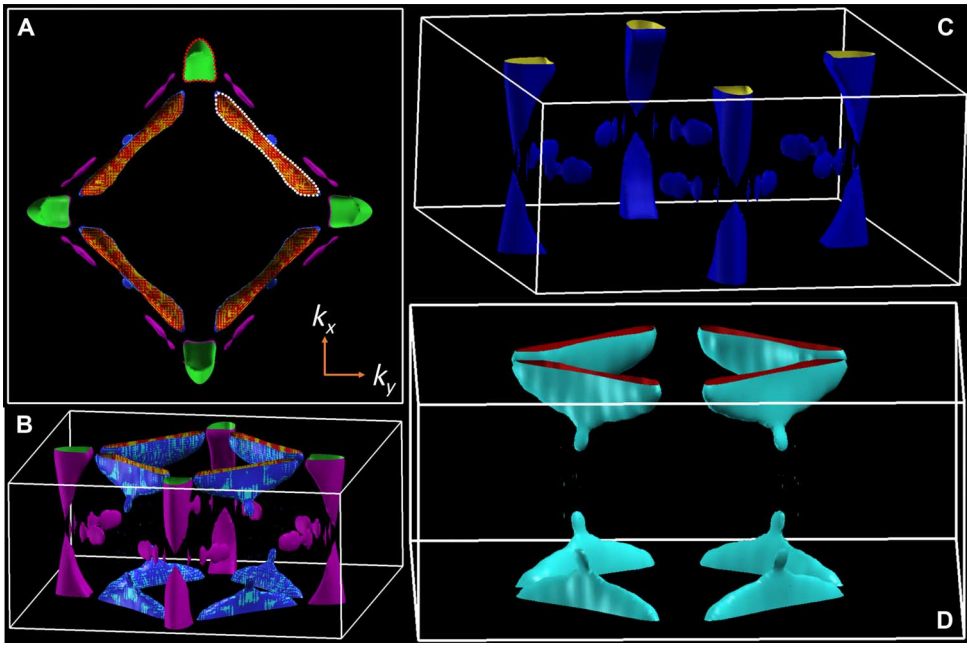

Fig. 1. Calculated Fermi surface for ZrSiS. (**A**) Projection of the merged band Fermi surface for ZrSiS, looking down the k_z axis. The sizes of two orbits easily identifiable from this projection (shown with dashed red and white lines, respectively) were extracted and found to be 2.24×10^{-2} and 4.52×10^{-2} Å^{-2}, respectively. The orbit highlighted in red corresponds to the more tubular feature, whereas the orbit highlighted in white corresponds to the diamond feature. (**B**) Canted view of the total Fermi surface showcasing the different types of pockets. (**C** and **D**) Two-band deconvoluted Fermi surface. The tubular feature and diamond contributions to the merged Fermi surface come from different bands (each existing twice due to spin-orbit coupling). Because of the diamond shape (which comes from the bands creating the Dirac line node), ZrSiS may exhibit nesting effects at low temperatures.

Our findings show that ZrSiS has a 2-K resistivity of 48(4) nΩ·cm, making it the most conductive sulfide known, stemming from its large concentration of high-mobility carriers. We also report the discovery of a butterfly-shaped titanic AMR effect in ZrSiS and a sharp, angle-dependent topological phase transition, when the current is applied along the *a* axis and an applied magnetic field is swept from along the *c* axis to the direction of the current. The butterfly AMR can be thought of as a convolution of two- and fourfold symmetric elements whose contributions change with temperature. At a low temperature, a "dip" in the MR beginning at 85° and maximizing at 90° is seen, which is coincident with sudden changes in both the linear and quadratic components of the MR. Analysis of the SdH oscillations identified several extremal orbits, which were found to shift remarkably with changing angle. One peak, at 243 T, shows a quasi-2D behavior by shifting like a $\approx 1/\cos(\theta)$ law, whereas another peak at 23 T shows a highly isotropic 3D behavior, not shifting at all. By analyzing DFT Fermi surface calculations, we found that the 243-T orbit was generated by the band crossing the Fermi energy along Γ-*X*, which also generates the nonsymmorphic point *X* and −0.5 eV. However, the primary result of this work is that between 85° and 95°, the 243-T orbit has a π Berry phase (extracted by fitting the resistivity oscillations to the Lifshitz-Kosevich formula), indicating a nontrivial topology, whereas by 80° (coincident with the dip in the AMR and change in the MR versus *H* behavior), the Berry phase suddenly changes to a trivial value, implying an angle-dependent topological phase transition. This type of sharp angle-dependent topological phase transition has not been theoretically predicted or reported in any other Dirac/Weyl material and is likely due to the quasi-2D nature of parts of the Fermi surface in ZrSiS. It has a markedly clear effect on MR, an unexpected but robust signature that is visible even though it is not the only contribution to transport, and may be used in devices where switching between Fermi surface types can be taken advantage of.

RESULTS

The zero-field temperature-dependent resistivity of ZrSiS is presented in Fig. 2A, and the residual resistivity at 2 K is shown in the inset. The current is applied along the *a* axis of the crystal. ZrSiS has an extremely low resistivity for a semimetal at room temperature, with a value of 15.5 μΩ·cm, falling to 48(4) nΩ·cm at 2 K and yielding a residual resistance ratio (RRR) of ≈300. At room temperature, other high-mobility semimetals (including Dirac and Weyl materials), such as Cd_3As_2, LaBi, and WTe_2, have resistivities at least one order of magnitude greater than the resistivity of ZrSiS (*3*, *4*, *16*). At low temperature, only Cd_3As_2 has a lower resistivity (21 nΩ·cm) than ZrSiS, which is comparable to that of high-purity Bi (*17*) and of oxides like $PdCoO_2$ (*18*). To the best of our knowledge, ZrSiS has the lowest resistivity of any sulfide known.

Figure 2B shows the curve of 9-T resistivity versus ZrSiS temperature at various angles of the applied field with respect to the current; 90° is defined as *H* being parallel to the *c* axis and perpendicular to *I*. The resistivity plateaus at low temperature at an angle of 50°, in a fashion similar to that of several high-mobility semimetals like WTe_2 (*16*), LaSb (*19*), and NbP (*4*) at 90°. However, at 60°, a maximum is visible, followed by a downturn in the resistivity. This sort of angle-dependent maximum has not been reported before in any Dirac/Weyl material or topological insulator. The inset shows the temperature-dependent Hall coefficient under various magnetic fields ($\theta = 90°$) in ZrSiS. The Hall coefficient peaks (p-type) at 100 K in a 1-T field before it rapidly decreases with decreasing temperature until it plateaus at 27 K, remaining

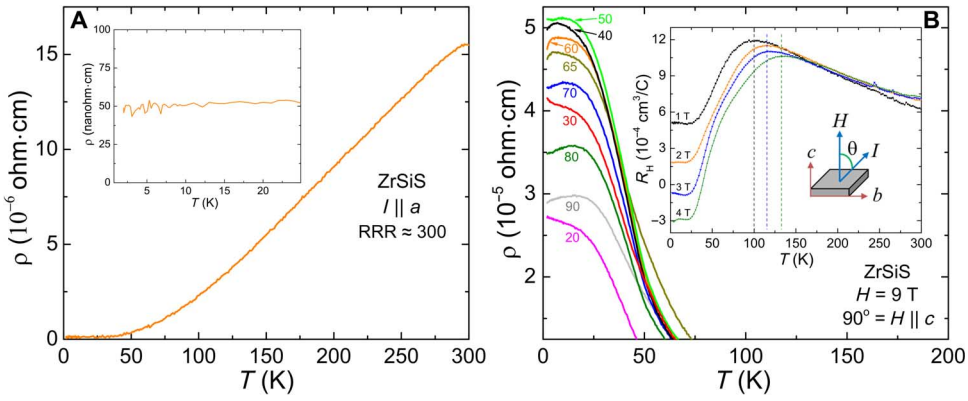

Fig. 2. Transport measurements on ZrSiS. (**A**) Zero-field temperature dependence of the resistivity in ZrSiS. The inset shows the extraordinarily low residual resistivity of 48(4) nΩ·cm for a crystal with an RRR of ≈300. (**B**) Temperature dependence (9 T) of the resistivity in ZrSiS at various angles. The θ value is taken as the angle between the applied field and the current, which is applied along the *a* axis. The inset shows the Hall resistance (*H* perpendicular to *I*) as a function of temperature at various magnetic fields. Dashed vertical lines show the magnetic field dependence of the maximum R_H. A p-n crossover is evident for the 3 and 4-T measurements at 30 and 39 K, respectively, before reaching a plateau at low temperatures.

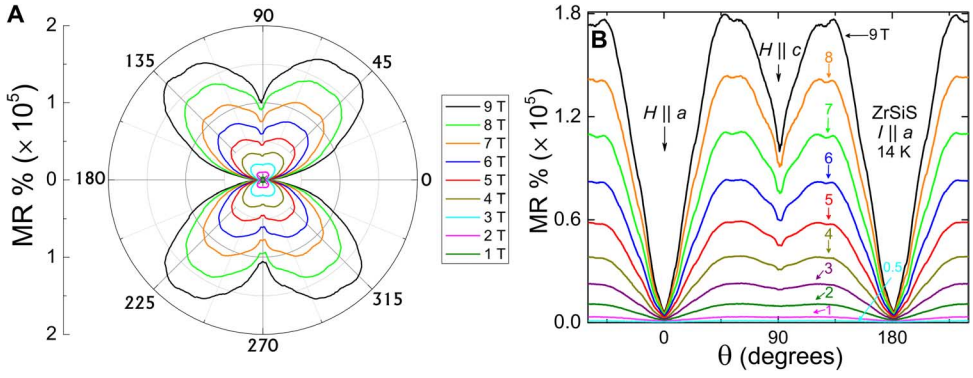

Fig. 3. AMR of ZrSiS. (**A**) Polar plot illustrating the butterfly AMR effect, coming from a convolution of two- and fourfold symmetry dependencies, taken at different applied magnetic field strengths. The θ value is taken as the angle between the applied field and the current, which is applied along the *a* axis. (**B**) Standard plot of the AMR showcasing the field strength–dependent dip in the MR, beginning at 85°, maximizing by 90°, and ending by 95°. Additional minor oscillatory components, on top of the two- and fourfold symmetry, and peak splitting around 45°, which also exhibits field strength dependence, are also present.

as p-type. The Hall peak moves to higher temperature with increasing magnetic field strength. Also, with stronger fields, a p-n crossover occurs at 30 K for a 3-T field and at 39 K for a 4-T field and stays as n-type down to 2 K.

The "butterfly" MR is presented in Fig. 3. Figure 3A shows AMR at various magnetic field strengths on a polar plot, whereas Fig. 3B shows a conventional plot. The polar plot illustrates the two- and fourfold symmetries as well as the dip occurring between 85° and 95°, which begins being evident by 4 T and becomes enhanced with increasing field. Figure S2B shows that the effect is the same when *H* is tilted from *c* toward *b*, instead of toward *a*. This butterfly pattern has been previously seen in the in-plane AMR of underdoped (antiferromagnetic), high-T_c superconductors, such as $Sr_{1-x}La_xCuO_2$ (*20*), and the anisotropic MR of rare earth manganates and other magnetic thin films (*21*, *22*). The phenomena present in ZrSiS cannot be ascribed the same origin due to the lack of magnetism in the compound. Elemental Bi, when *H* is rotated in plane, exhibits a sixfold symmetry in its AMR stemming from its three in-plane ellipsoidal pockets and a breakdown of symmetry in higher magnetic fields (*23*, *24*). Recently, LaBi (*25*) was shown to have a fourfold MR dependence; however, neither the dip in the MR around 90° nor the higher order texturing found in ZrSiS (visible in Fig. 3B) appears to be present in LaBi. The standard plot reveals the higher order texturing, such as the splitting of the peak near 45° into two unequal maxima, in the AMR that clearly does not belong to either two- or fourfold symmetry components. In some layered metals and semiconductors, these AMR oscillations (AMROs) were interpreted as the Aharonov-Bohm effect in real and momentum spaces (*26*). Further investigation of the AMRO of ZrSiS will elucidate the subtleties of the Fermi surface.

The AMR was measured at several different temperatures to gain insight into the temperature dependence of the effect. By fitting the AMR to a simple convolution of the two symmetries, $p_1 \sin(\theta)^2 + p_2 \sin(2\theta)^2 + 1$, the relative weights of the two- and fourfold components were extracted. This fitting was done for each magnetic field strength (0.5 to 9 T) at several different temperatures (14, 20, 25, 30, 50, and 70 K) (see the Supplementary Materials). The extracted weights are plotted versus field strength for each temperature (fig. S3). At 14 K, the twofold component dominates over the fourfold component until high field (≈8.5 T); however, as the temperature increases, the fourfold component dies off faster than does the twofold component, implying that the cause of the fourfold component is distinct from that of the twofold component.

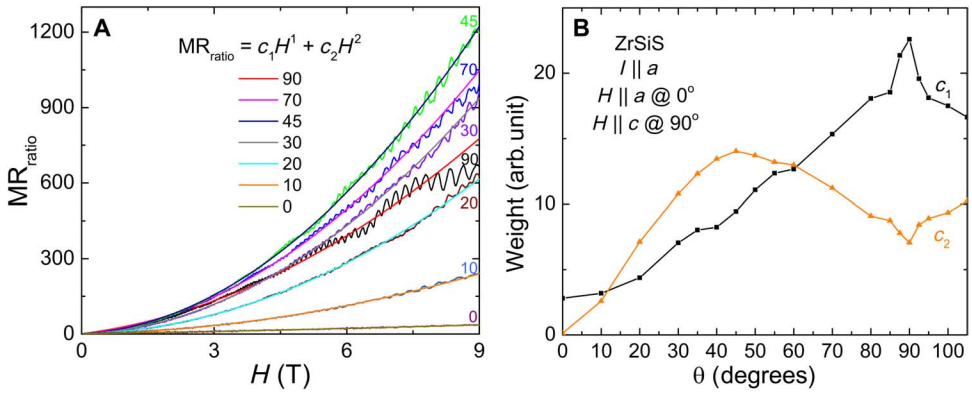

Fig. 4. MR as a function of applied field at various angles in ZrSiS. (**A**) MR versus $\mu_0 H$ at various angles (full data in the Supplementary Materials) along with fits to $MR = 1 + c_1 H + c_2 H^2$, where c_1 and c_2 are the relative weights given to the linear and quadratic terms of the equation. Solid, smooth lines are the fits, whereas oscillating lines are the data. (**B**) Extracted c_1 and c_2 dependencies from the full 9-T MR versus H curves taken at 0°, 10°, 20°, 30°, 35°, 40°, 45°, 50°, 55°, 60°, 70°, 80°, 85°, 87.5°, 90°, 92.5°, 95°, 100°, and 105°, where θ is taken as the angle between the applied field and the current, which is applied along the a axis. Solid squares and solid triangles are the extracted values for c_1 and c_2, respectively.

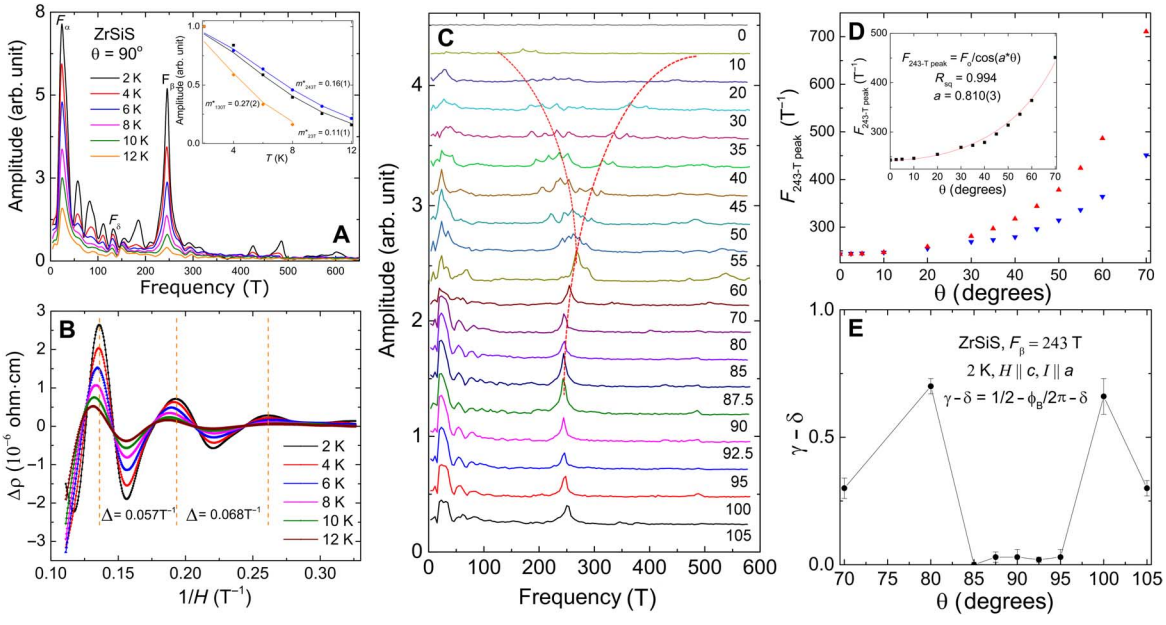

Fig. 5. Quantum oscillation analysis and extraction of the Berry phase in ZrSiS. (**A**) FFT at 90° of the SdH oscillations extracted after subtracting a polynomial background (see the Supplementary Materials). F_α, F_β, and F_δ denote frequencies at 23, 243, and 130 T, respectively. Extra peaks resulting from $F_{2\alpha}$, $F_{3\alpha}$, $F_{4\alpha}$, and $F_{2\beta}$ are also visible along with three more unidentified frequencies at 154, 186, 426, and 487 T. The inset shows the LK fit used to determine the effective mass of the electrons for the 23-, 243-, and 130-T peaks. (**B**) Deconvoluted oscillations pertaining to the F_α. Dashed lines indicate the apparent decay of the period of the oscillation with decreasing field and showcase the temperature-dependent shift of the oscillation's maxima, making the phase analysis of F_α extremely unreliable. (**C**) FFT from the extracted oscillations at many different angles of the applied field. Curved lines are guides to the eye to illustrate the peak splitting and shifting occurring as a function of the angle of the applied field. (**D**) Angular dependence of the F_β peak. Here, the definition of θ was rotated 90° to allow for easier comparison with other materials; θ = 0 is H parallel to c. Red triangles are the expected values for a truly 2D pocket following the 1/cos(θ) law, inverted blue triangles are the measured values, and a deviation occurs by 20°. The inset shows a fit of the data to $F/B\cos(a^*\theta)$. (**E**) Extracted total phase ($\gamma - \delta$) of F_β as a function of angle, obtained by fitting the LK formula to the deconvoluted F_β's SdH oscillations. See the Supplementary Materials for details.

To investigate the dip around 90°, we measured the MR versus field strength at many different angles at 2 K. Figure 4A shows the MR for selected angles and the fit of the nonoscillatory background to a combination of a linear and quadratic component; $MR_{ratio} = c_1 H^1 + c_2 H^2$. This was used because although the MR increases in a nearly quadratic fashion at 45° (as seen for WTe_2), the MR is subquadratic by 90°. Linear MR was seen for other Dirac materials, such as Na_3Bi and Cd_3As_2 (*2*, *3*), and can be caused by a variety of reasons, including the presence of Dirac-like charge carriers (*27*). c_1 and c_2 are the relative weights of each component and are plotted versus angle in Fig. 4B. When H is parallel to I, the MR increases in an almost entirely linear fashion with increasing magnetic field, but the quadratic component begins to dominate very quickly (by 12°). The weight of the quadratic component increases by more than two orders of

magnitude at 45° (from 0.13 to 14), whereas the linear component increases only by a factor of 8 by 90°. Exactly in the regime where the dip became evident in the AMR, the quadratic term suddenly dips, whereas the linear term spikes upward (between 85° and 90°). To be sure that it was not an artifact, measurements were taken beyond 90°, and the expected symmetry was seen. The sudden minimization in the quadratic component is on top of an already fourfold symmetry, whereas the spike in the linear component is on top of an apparent twofold symmetry, again implying different origins for each contribution.

By extracting the SdH oscillations from the various MR versus H loops (see the Supplementary Materials for methodology), the origin of the sudden change in the linear and quadratic contributions was investigated. Figure 5A shows the fast Fourier transform (FFT) of the SdH oscillations taken at 90° and at various different temperatures. F_α denotes a peak at 23 T, F_β at 243 T, and F_δ at 130 T. The $F_{2\alpha}$, $F_{3\alpha}$, and $F_{4\alpha}$ and the $F_{2\beta}$ harmonics are also visible. With the Lifshitz-Kosevich temperature reduction formula (*28*–*30*), the effective masses for the three pockets were found (inset) to be 0.11, 0.16, and 0.27 × m_e, respectively. Correspondingly, the areas of the Fermi surface for the three orbits are 2.2×10^{-3}, 2.3×10^{-2}, and 1.2×10^{-2} A^{-2}, with small K_F sizes of 2.6×10^{-2}, 8.6×10^{-2}, and 6.3×10^{-2} A^{-1}, respectively (see the Supplementary Materials). The area of the 243-T peak corresponds well (agreement to within 95%) with the area of the theoretically calculated extremal orbit previously discussed (Fig. 1; the orbit belonging to the tubular feature). The Fermi velocities are quite large, at 2.8×10^5, 6.3×10^5, and 2.7×10^5 m/s, respectively, comparable to Cd_3As_2, WTe_2, and LaBi. However, the orbit giving rise to F_α is very close in size to another similar orbit (visible in the 50° and 55° FFTs), resulting in a convoluted peak with a broadened shape. Figure 5B shows how the period of F_α appears to decay with decreasing field strength and that the positions of the maxima shift slightly with increasing temperature ($H \parallel c$). Figure 5C shows the FFT of the SdH oscillations at various angles. Between 60° and 50°, F_α splits into two nearby peaks before it returns to a single peak behavior by 45°. The 243-T peak is sharp and can be seen shifting to higher frequencies until 55°, at which point several new peaks become visible and shift in different directions with decreasing angle. The red dashed line shows that F_β can be followed in its shift through the 20° data. A 2D Fermi surface, when tilted with respect to an applied magnetic field, has a peak shift following the $\approx 1/\cos(\theta)$ law (*25*, *31*). Figure 5D shows the frequency of F_β as a function of the angle; at larger angles, while still following the habit of a $1/\cos(\theta)$ dependence, the peak does not shift as much as expected for a truly 2D Fermi surface. The inset is a fit of the data to a 1/cos function with a larger period; in a perfectly 2D Fermi surface, a would be 1 and deviation from this can be considered a measure of the "3D" aspect of the pocket. Because the F_β's shift deviates from the 1/cos law between 20° and 30° and because the shifts can be fit with $a = 0.81$, the F_β oscillation stems from a quasi-2D surface. On the other hand, the F_α peak shows almost no shift for over a 50° range, implying that it comes from a 3D and highly isotropic feature in the Fermi surface.

Because of the singular nature of F_β near 90°, it was possible to extract the Berry phase of the orbit by directly fitting the oscillations using the following formula: $\rho_{xx} = \rho_0[1 + A(B,T)\cos 2\pi(B_F/B - \delta + \gamma)]$ (*3*, *29*, *32*–*34*). Here, $1/B_F$ is the SdH frequency and is a phase shift determined by the dimensionality of the feature: 0 for the 2D case and –1/8 for the 3D case (for electrons). The Berry phase is related via $|\gamma - \delta| = |1/2 - \phi_B/2\pi - \delta|$; values for $|\gamma - \delta|$, which imply a nontrivial π Berry phase, are 0 and 1/8 for the 2D and 3D cases, respectively. Figure 5E shows the extracted $|\gamma - \delta|$ for F_β between 70° and 105°. Between 85° and 95°, $|\gamma - \delta|$ is very close to 0; a slight deviation of 0.03 is likely caused by the quasi-2D nature of the pocket δ, causing it to not be exactly 0 but instead taking on an intermediate value between 0 and 1/8. As the field is tilted away from the c axis, a sudden change in $|\gamma - \delta|$ is seen between 85° and 80°. $|\gamma - \delta|$ takes on a value of 0.7, which is too large of a change to solely be coming from a change in δ. This requires that the Berry phase also changes to a value other than π, implying a transition to a trivial topology.

DISCUSSION

Figure S5A shows the deconvoluted data for F_β, showcasing the sudden and visible difference in phase of the oscillations by 80°. A Landau fan diagram was also used to check for agreement with the direct LK fit (fig. S5B). Although Cd_3As_2 has a smooth change in the Berry phase of its ellipsoidal pocket with a changing angle (*35*, *36*), this type of sharp, angle-dependent topological phase transition has not been reported in any other Dirac/Weyl material (nor has it been predicted to exist by theoretical analysis) and is likely due to the quasi-2D nature of the feature. According to DFT calculations, two bands make up the bulk Fermi surface, with one band comprising the diamond shape and representing the Dirac line node. The line node is only protected at $k_z = 0$ and π; hence, it does not create a 2D pocket because there are k_z values where the pocket vanishes. The other band cuts the Fermi energy along the Γ-X line and is more tubular-shaped (along k_z), being more 2D. This feature generates the 243-T orbit (identified by matching the theoretical orbital size with the experimentally measured orbits). This pocket also belongs to the band that connects to the nonsymmorphic point X at lower energies and cuts the Fermi level along the Γ-X line as well as the Z-R line.

The marked effect of the phase transition on the MR makes it noticeable in a bulk transport property of an extremely conductive semimetal, an unexpected but robust signature that can be seen, although there are contributions from other parts of the Fermi surface. It is highly unlikely that the effect is related to surface state transport; the bulk conductivity of the material makes isolating surface state effects from bulk transport effects extremely difficult in the current experiment. A transition like this, which is highly sensitive and depends only on a 10° or less change in the magnetic field angle, opens the door to creating new types of devices based on subtle details of the Fermi surface. A simple Fermitronic device, consisting of a layer of a material like ZrSiS topped by a ferromagnetic layer whose magnetization direction can be adjusted using voltage-controlled magnetic anisotropy or spin torque (*37*–*39*), can be envisioned to switch between topological states. However, information on the state is currently buried deep within MR versus H measurements. A method to probe the topological state in a less intensive way is needed. However, if combined with a device based on switching between topological states, it could give rise to an entirely new type of logic device. ZrSiS is a rich system for fundamental study; the low-temperature, high-field behavior of the resistivity as well as many aspects of the AMR are still unexplained. However, because the Fermi surface is made from Dirac bands, it is likely that the peculiar behaviors have a nontrivial origin and will benefit from careful theoretical analysis of the electronic structure, which may be key in potentially unlocking further properties of interest. ZrSiS is also an exciting system for technological applications because of its low resistivity; sensitive Fermi surface; cheap, nontoxic, and earth-abundant chemical makeup; and relatively easy

synthesis. Future work on thin-film fabrication and chemically doped samples may lead to exciting possibilities for Fermitronic devices as well as for probing the unusual surface state. Higher magnetic field AMR measurements coupled with optical experiments may provide valuable insight into the various contributions of the Fermi surface of ZrSiS to its electrical properties.

MATERIALS AND METHODS

Single crystals were grown from the mixed elements via I_2 vapor transport at 1100°C, with a 100°C temperature gradient. The crystals were obtained at the cold end and then annealed in a sealed quartz tube for 1 week at 700°C.

ZrSiS crystals were structurally and chemically characterized by powder x-ray diffraction (XRD) to confirm bulk purity, single-crystal XRD to determine crystal growth orientation, scanning electron microscopy–energy-dispersive x-ray for chemical analysis, and transmission electron microscopy. The Quantum Design Physical Property Measurement System was used for transport measurements with ac transport and resistivity options. Hall measurements were taken in a five-wire configuration, whereas the MR of ZrSiS samples was measured using the four-point probe method. Because of the extremely low resistivity of the crystals, mechanical polishing was done to thin the samples down to 70 μm to obtain low-noise measurements.

The electronic structure calculations were performed in the framework of DFT using the WIEN2k (*40*) code with a full-potential linearized augmented plane-wave and local orbitals (FP-LAPW + lo) basis (*41*), together with the Perdew-Burke-Ernzerhof parametrization of the generalized gradient approximation as the exchange-correlation functional. The Fermi surface was plotted with the *XCrySDen* program.

SUPPLEMENTARY MATERIALS

Supplementary material for this article is available at http://advances.sciencemag.org/cgi/content/full/2/12/e1601742/DC1

fig. S1. Powder x-ray diffraction pattern for ground single crystals of ZrSiS.
fig. S2. AMR measured in other principal directions along with symmetry fitting.
fig. S3. Extracted weights from AMR fitting.
fig. S4. Quantitative quantum oscillation analysis using band pass filtration.
fig. S5. Direct Lifshitz-Kosevich fitting compared with Landau Level fan diagram.
References (*42*–*44*)

REFERENCES AND NOTES

1. M. N. Ali, J. Xiong, S. Flynn, J. Tao, Q. D. Gibson, L. M. Schoop, T. Liang, N. Hal-dolaarachchige, M. Hirschberger, N. P. Ong, R. J. Cava, Large, non-saturating magnetoresistance in WTe_2.*Nature* **514**, 205–208 (2014).
2. J. Xiong, S. K. Kushwaha, T. Liang, J. W. Krizan, M. Hirschberger, W. Wang, R. Cava, N. P. Ong, Evidence for the chiral anomaly in the Dirac semimetal Na_3Bi.*Science* **350**, 413–416 (2015).
3. T. Liang, Q. Gibson, M. N. Ali, M. Liu, R. J. Cava, N. P. Ong, Ultrahigh mobility and giant magnetoresistance in the Dirac semimetal Cd_3As_2. *Nat. Mater.* **14**, 280–284 (2015).
4. C. Shekhar, A. K. Nayak, Y. Sun, M. Schmidt, M. Nicklas, I. Leermakers, U. Zeitler, W. Schnelle, J. Grin, C. Felser, B. Yan, Extremely large magnetoresistance and ultrahigh mobility in the topological Weyl semimetal NbP. arXiv:1502.04361 (2015).
5. X. Huang, L. Zhao, Y. Long, P. Wang, D. Chen, Z. Yang, H. Liang, M. Xue, H. Weng, Z. Fang, X. Dai, G. Chen, Observation of the chiral-anomaly-induced negative magnetoresistance in 3D Weyl semimetal TaAs. *Phys. Rev. X* **5**, 031023 (2015).
6. J. Hu, Z. Tang, J. Liu, X. Liu, Y. Zhu, D. Graf, K. Myhro, S. Tran, C. N. Lau, J. Wei, Z. Mao, Evidence of topological nodal-line fermions in ZrSiSe and ZrSiTe. *Phys. Rev. Lett.* **117**, 016602 (2016).
7. Y. Wu, L.-L. Wang, E. Mun, D. D. Johnson, D. Mou, L. Huang, Y. Lee, S. L. Bud'ko, P. Canfield, A. Kaminski, Dirac node arcs in $PtSn_4$. *Nat. Phys.* **12**, 667–671 (2016).
8. N. W. Ashcroft, N. D. Mermin, *Solid State Physics* (Brooks and Cole, 1976).
9. N. Doiron-Leyraud, C. Proust, D. LeBoeuf, J. Levallois, J.-B. Bonnemaison, R. Liang, D. A. Bonn, W. N. Hardy, L. Taillefer, Quantum oscillations and the Fermi surface in an underdoped high-T_c superconductor. *Nature* **447**, 565–568 (2007).
10. Z. Zhu, A. Collaudin, B. Fauqué, W. Kang, K. Behnia, Field-induced polarization of Dirac valleys in bismuth. *Nat. Phys.* **8**, 89–94 (2011).
11. L. R. Thoutam, Y. L. Wang, Z. L. Xiao, S. Das, A. Luican-Mayer, R. Divan, G. W. Crabtree, W. K. Kwok, Temperature-dependent three-dimensional anisotropy of the magnetoresistance in WTe_2. *Phys. Rev. Lett.* **115**, 046602 (2015).
12. L. M. Schoop, M. N. Ali, C. Straßer, A. Topp, A. Varykhalov, D. Marchenko, V. Duppel, S. S. P. Parkin, B. V. Lotsch, C. R. Ast, Dirac cone protected by non-symmorphic symmetry and three-dimensional Dirac line node in ZrSiS. *Nat. Commun.* **7**, 11696 (2016).
13. Q. Xu, Z. Song, S. Nie, H. Weng, Z. Fang, X. Dai, Two-dimensional oxide topological insulator with iron-pnictide superconductor LiFeAs structure. *Phys. Rev. B* **92**, 205310 (2015).
14. R. Singha, A. Pariari, B. Satpati, P. Mandal, Titanic magnetoresistance and signature of non-degenerate Dirac nodes in ZrSiS. arXiv:1602.01993 (2016).
15. Y.-Y. Lv, B.-B. Zhang, X. Li, S.-H. Yao, Y. B. Chen, J. Zhou, S.-T. Zhang, M.-H. Lu, Y.-F. Chen, Extremely large and significantly anistropic magnetoresistance in ZrSiS single crystals. arXiv:1604.01864 (2016).
16. M. N. Ali, L. Schoop, J. Xiong, S. Flynn, Q. Gibson, M. Hirschberger, N. P. Ong, R. J. Cava, Correlation of crystal quality and extreme magnetoresistance of WTe_2. *EPL* **110**, 67002 (2015).
17. P. B. Alers, R. T. Webber, The magnetoresistance of bismuth crystals at low temperatures. *Phys. Rev.* **91**, 1060 (1953).
18. C. W. Hicks, A. S. Gibbs, A. P. Mackenzie, H. Takatsu, Y. Maeno, E. A. Yelland, Quantum oscillations and high carrier mobility in the delafossite $PdCoO_2$. *Phys. Rev. Lett.* **109**, 116401 (2012).
19. F. F. Tafti, Q. D. Gibson, S. K. Kushwaha, N. Haldolaarachchige, R. J. Cava, Resistivity plateau and extreme magnetoresistance in LaSb. *Nat. Phys.* **12**, 272–277 (2016).
20. V. P. Jovanović, L. Fruchter, Z. Z. Li, H. Raffy, Anisotropy of the in-plane angular magnetoresistance of electron-doped Sr 1_{-x} La_x CuO_2 thin films. *Phys. Rev. B* **81**, 134520 (2010).
21. Y. Q. Zhang, H. Meng, X. W. Wang, X. Wang, H. H. Guo, Y. L. Zhu, T. Yang, Z. D. Zhang, Angular dependent magnetoresistance with twofold and fourfold symmetries in A-type antiferromagnetic $Nd_{0.45}Sr_{0.55}MnO_3$ thin film. *Appl. Phys. Lett.* **97**, 172502 (2010).
22. K. Mukherjee, S. D. Das, N. Mohapatra, K. K. Iyer, E. V. Sampathkumaran, Anomalous butterfly-shaped magnetoresistance loops in the alloy Tb_4LuSi_3. *Phys. Rev. B* **81**, 184434 (2010).
23. Z. Zhu, A. Collaudin, B. Fauqué, W. Kang, K. Behnia, Field-induced polarization of Dirac valleys in bismuth. *Nat. Phys.* **8**, 89–94 (2012).
24. A. Collaudin, B. Fauqué, Y. Fuseya, W. Kang, K. Behnia, Angle dependence of the orbital magnetoresistance in bismuth. *Phys. Rev. X* **5**, 021022 (2015).
25. N. Kumar, C. Shekhar, S.-C. Wu, I. Leermakers, U. Zeitler, B. Yan, C. Felser, Observation of pseudo two dimensional electron transport in the rock salt type topological semimetal LaBi. arXiv:1601.07494 (2016).
26. V. M. Yakovenko, B. K. Cooper, Angular magnetoresistance oscillations in bilayers in tilted magnetic fields. *Phys. E Low Dimens. Syst. Nanostruct.* **34**, 128–131 (2006).
27. J. Hu, T. Rosenbaum, Classical and quantum routes to linear magnetoresistance. *Nat. Mater.* **7**, 697–700 (2008).
28. Y. Qi, P. G. Naumov, M. N. Ali, C. R. Rajamathi, W. Schnelle, O. Barkalov, M. Hafland, S.-C. Wu, C. Shekhar, Y. Sun, V. Süβ, M. Schmidt, U. Schwarz, E. Pippel, P. Werner, R. Hillebrand, T. Förster, E. Kampert, S. Parkin, R. J. Cava, C. Felser, B. Yan, S. A. Medvedev, Superconductivity in Weyl semimetal candidate $MoTe_2$. *Nat. Commun.* **7**, 11038 (2016).
29. H. Murakawa, M. S. Bahramy, M. Tokunaga, Y. Kohama, C. Bell, Y. Kaneko, N. Nagaosa, H. Y. Hwang, Y. Tokura, Detection of Berry's phase in a bulk Rashba semiconductor. *Science* **342**, 1490–1493 (2013).
30. Y. Luo, N. J. Ghimire, M. Wartenbe, H. Choi, M. Neupane, R. D. McDonald, E. D. Bauer, J. Zhu, J. D. Thompson, F. Ronning, Electron-hole compensation effect between topologically trivial electrons and nontrivial holes in NbAs. *Phys. Rev. B* **92**, 205134 (2015).
31. D.-X. Qu, Y. S. Hor, J. Xiong, R. Cava, N. P. Ong, Quantum oscillations and hall anomaly of surface states in the topological insulator Bi_2Te_3. *Science* **329**, 821–824 (2010).
32. V. Tayari, N. Hemsworth, I. Fakih, A. Favron, E. Gaufrès, G. Gervais, R. Martel, T. Szkopek, Two-dimensional magnetotransport in a black phosphorus naked quantum well. *Nat. Commun.* **6**, 7702 (2015).
33. J. Hu, J. Y. Liu, D. Graf, S. M. A. Radmanesh, D. J. Adams, A. Chuang, Y. Wang, I. Chiorescu, J. Wei, L. Spinu, Z. Q. Mao, π Berry phase and Zeeman splitting of Weyl semimetal TaP. *Sci. Rep.* **6**, 18674 (2016).
34. G. Mikitik, Y. V. Sharlai, Manifestation of Berry's phase in metal physics. *Phys. Rev. Lett.* **82**, 2147 (1999).
35. J. Cao, S. Liang, C. Zhang, Y. Liu, J. Huang, Z. Jin, Z.-G. Chen, Z. Wang, Q. Wang, J. Zhao, S. Li, X. Dai, J. Zou, Z. Xia, L. Li, F. Xiu, Landau level splitting in Cd_3As_2 under high magnetic fields. *Nat. Commun.* **6**, 7779 (2015).
36. Y. Zhao, H. Liu, C. Zhang, H. Wang, J. Wang, Z. Lin, Y. Xing, H. Lu, J. Liu, Y. Wang, S. M. Brombosz, Z. Xiao, S. Jia, X. C. Xie, J. Wang, Anisotropic Fermi surface and quantum limit transport in high mobility three-dimensional Dirac semimetal Cd_3As_2. *Phys. Rev. X* **5**, 031037 (2015).

37. Y. Shiota, T. Nozaki, F. Bonell, S. Murakami, T. Shinjo, Y. Suzuki, Induction of coherent magnetization switching in a few atomic layers of FeCo using voltage pulses. *Nat. Mater.* **11**, *39*–43 (2012).
38. W.-G. Wang, M. Li, S. Hageman, C. L. Chien, Electric-field-assisted switching in magnetic tunnel junctions. *Nat. Mater.* **11**, 64–68 (2012).
39. D. C. Ralph, M. D. Stiles, Spin transfer torques. *J. Magn. Magn. Mater.* **320**, 1190–1216 (2008).
40. P. Blaha, K. Schwarz, G. Madsen, D. Kvasnicka, J. Luitz, *WIEN2k, An Augmented Plane Wave+ Local Orbitals Program for Calculating Crystal Properties* (Technische Universität Wien, 2001).
41. D. J. Singh, L. Nordström, *Planewaves, Pseudopotentials, and the LAPW Method* (Springer, ed. 2, 2006).
42. A. V. Oppenheim, R. W. Schafer, *Discrete-Time Signal Processing* (Pearson Higher Education, ed. 3, 2010).
43. F. Gustafsson, Determining the initial states in forward-backward filtering. *IEEE Trans. Signal Process.* **44**, 988–992 (1996).
44. S. K. Mitra, Y. Kuo, *Digital Signal Processing: A Computer-Based Approach* (McGraw-Hill, 2006).

Acknowledgments: We acknowledge T. Phung and A. Rost for useful discussions. **Funding:** This research was supported by IBM Research, the Max Planck Institute (MPI) of Microstructure Physics, the MPI for Solid State Research, and the Nanosystems Initiative Munich and Center for Nanoscience. **Author contributions:** M.N.A. led the research investigation and measured the transport data. L.M.S. and J.M.L. developed the crystal growth procedure and grew the samples. L.M.S. carried out the electronic structure calculations. C.G. and M.N.A. conducted the data analysis. E.L. assisted in preparing the experiments. All authors assisted in interpreting the results and placing them into context. B.L. and S.S.P.P. are the principal investigators. **Competing interests:** The authors declare that they have no competing interests. **Data and materials availability:** All data needed to evaluate the conclusions in the paper are present in the paper and/or the Supplementary Materials. Correspondence and requests for materials should be addressed to M.N.A. (maz@berkeley.edu).

Submitted 26 July 2016
Accepted 15 November 2016
Published 16 December 2016
10.1126/sciadv.1601742

Citation: M. N. Ali, L. M. Schoop, C. Garg, J. M. Lippmann, E. Lara, B. Lotsch, S. S. P. Parkin, Butterfly magnetoresistance, quasi-2D Dirac Fermi surface and topological phase transition in ZrSiS. *Sci. Adv.* **2**, e1601742 (2016).

ScienceAdvances
AAAS

Butterfly magnetoresistance, quasi-2D Dirac Fermi surface and topological phase transition in ZrSiS

Mazhar N. Ali, Leslie M. Schoop, Chirag Garg, Judith M. Lippmann, Erik Lara, Bettina Lotsch and Stuart S. P. Parkin

(December 16, 2016)
Sci Adv 2016, 2:.
doi: 10.1126/sciadv.1601742